Fluid flow over and through a regular bundle of rigid fibres

Giuseppe A. Zampogna[1] and Alessandro Bottaro[1,†]

[1]DICCA, Scuola Politecnica, Università di Genova, via Montallegro 1, 16145 Genova, Italy

The interaction between a fluid flow and a transversely isotropic porous medium is described. A homogenized model is used to treat the flow field in the porous region, and different interface conditions, needed to match solutions at the boundary between the pure fluid and the porous regions, are evaluated. Two problems in different flow regimes (laminar and turbulent) are considered to validate the system, which includes inertia in the leading-order equations for the permeability tensor through a Oseen approximation. The components of the permeability, which characterize microscopically the porous medium and determine the flow field at the macroscopic scale, are reasonably well estimated by the theory, both in the laminar and the turbulent case. This is demonstrated by comparing the model's results to both experimental measurements and direct numerical simulations of the Navier–Stokes equations which resolve the flow also through the pores of the medium.

Key words: low-Reynolds-number flows, porous media

---

1. Introduction

Flows in porous media are common in nature and in technical applications, with velocities through the pores which range from very low values (e.g. flow in biological tissues, ground water infiltration) to very large (e.g. canopy flow). When a fluid flows in a porous medium, there is usually a strong separation of scales between the macroscopic scale defined by the global size of the problem and the microscopic length typical of the solid inclusions of the porous medium (cf. figure 1). Two approaches are generally used to treat this type of phenomenon: the first one is to implement a pore-scale numerical simulation of the flow in the medium, reproducing closely the geometry of the solid skeleton. The second consists in an effective macroscopic simulation where the microscopic structure is lost, but some auxiliary problem is introduced to characterize the pore-scale behaviour. The first path has been followed, for instance, by Breugem & Boersma (2005), Kuttanikkad (2009) and Matsumura & Jackson (2014). One of the difficulties of this kind of analysis is the computational cost of the simulation: the smaller is the ratio between the microscopic and the macroscopic length scale, the larger is the resolution which must be used to discretize the geometry of the skeleton. Such a big effort presents the additional disadvantage of providing a solution to only a particular configuration of

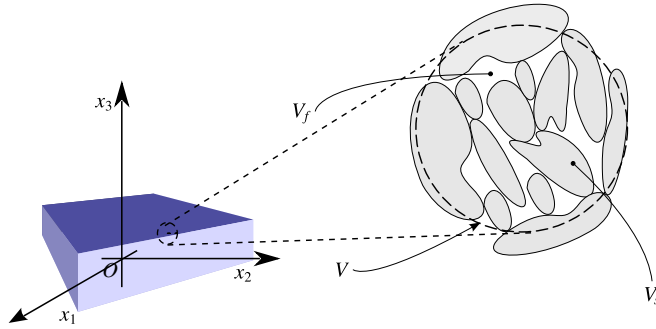† Email address for correspondence: alessandro.bottaro@unige.it

FIGURE 1. (Colour online) View of a generic porous medium within an elementary cell V. V_f is the volume occupied by the fluid and V_s is that occupied by the solid, so that $V = V_f + V_s$. Γ is the fluid–solid microscopic interface.

the porous medium. With the second choice we have a concise and rapid description of the fluid behaviour, satisfactory from a macroscopic point of view. A precursory idea of this method consists in assuming that simulating a fluid flowing through a porous medium is the same as thinking of the coupled fluid–solid medium as a continuum for which an effective conductivity, permeability or viscosity, different from that of the fluid, can be defined. These effective medium approaches were first postulated from an empirical point of view by Darcy (1856) and then modified using analytical considerations (Brinkman 1949). Even if the equations were born as empirical laws, several strategies have been developed in time in order to derive these equations analytically, deducing the macroscopic behaviour from the local description (see Davit *et al.* 2013, for a review). This procedure is called upscaling. Different techniques are available for upscaling: they start from a representative elementary volume (REV) and generate an equivalent macroscopic continuous model called the homogenized model. One of the most used approaches is the volume averaging method thoroughly described by Whitaker (1998). It consists in considering an elementary cell representative of the porous structure (V in figure 1); the size of the REV is of the order of the pore size. A fundamental assumption is that of periodicity, over V, for the unknown quantities. Starting from the Navier–Stokes equations (NSE), it is assumed that the solution (velocity and pressure fields) can be decomposed into a mean part plus a fluctuation (Gray 1975). The fluctuation represents how much the solution is far from its mean part and it must satisfy a zero average condition over the REV, that is fundamental to deduce the effective equations. After substituting the decomposition of the unknown fields inside the NSE, and considering the spatial average of the equations over the REV, one obtains the momentum equation for the mean flow, with forcing terms related to the fluctuations. In this way, the Darcy's law (Whitaker 1986), its Brinkman's correction (Quintard & Whitaker 1994) and the Forchheimer's equation (Whitaker 1996) have been deduced theoretically.

Another strategy widely used is described by Mei & Vernescu (2010) and consists in implementing a homogenization technique based on a multiple scale analysis. The starting point of this technique is the same as the volume averaging method: the NSE are taken to be valid over V_f in figure 1 and a proper expansion of the unknown fields is assumed. If the convective term is sufficiently small (of the order of the ratio between length scales) the resulting equations at leading order are self-contained, i.e. there is no need to introduce a closure relation. Darcy's,

Brinkman's and Forchheimer's equations can be deduced analytically also in this case. Both approaches briefly outlined above require closure relations when nonlinear terms are present. Much work is present in the literature: in particular, Mei & Auriault (1991) have examined the effect of weak fluid inertia in the porous medium, finding that Forchheimer's correction to Darcy's law should be at least cubic (instead of quadratic) for isotropic media. This has been confirmed by Firdaouss, Guermond & Le Quéré (1997). The same occurs for orthotropic media (Skjetne & Auriault 1999). Auriault (2009) investigated the domain of validity of Brinkman's equation, finding that it is valid for swarms of fixed particles or a fixed bed of fibres at very low concentration and under precise conditions which depend on the separation of the scale parameter $\epsilon = l/L$, with l and L two different representative length scales.

Homogenization provides a point of contact between the microscopic and the macroscopic worlds, and permits to transfer information from one point of view to the other. In this, it differs from purely microscopic approaches such as those by Jackson & James (1986), van der Westhuizen & du Plessis (1996), Tamayol & Bahrami (2009) and Yazdchi *et al.* (2011), and it is also different from purely macroscopic points of view, such as that by Battiato (2012) in which analytical forms of the permeability are taken from the literature.

All the works and the methods cited up to now refer to the solution of the flow deeply inside a porous medium, far from the boundaries. The problem of the interface conditions between the pure fluid and the porous region is crucial and amply discussed in the literature. Jäger & Mikelić (1996, 2000) spent much effort on this problem, concluding, through functional analysis and introducing an auxiliary problem based on homogenization, that the widely used condition of Beavers & Joseph (1967) and its modification by Saffman (1971) have a mathematical justification. Beavers & Joseph (1967) observed that the penetration of the velocity into the porous bed extends over a length proportional to $\sqrt{\mathscr{K}}$, with $\mathscr{K}$ the bed's permeability. This is equivalent to specifying a jump in the average velocity at the interface. More elaborate conditions have also been proposed, simulating the flow inside the porous medium with the Darcy–Brinkman equation, introducing an effective viscosity μ_e (which can be evaluated experimentally, see Givler & Altobelli 1994), and imposing continuity of the normal and tangential components of the stress tensor at the interface (Hill & Straughan 2008). Another interface condition has been developed by Ochoa-Tapia & Whitaker (1995) via the definition of the excess surface and bulk stress tensors to be obtained from the governing equations holding in the porous and pure fluid regions. This condition becomes, under certain hypotheses, the continuity of the effective velocity and pressure over the macroscopic interface. Finally, a strategy often used to couple two different media is the penalization method. It consists in solving the NSE in the whole domain, with a forcing term added in the porous region to take into account the presence of the structure. This forcing term is multiplied by the characteristic equation of the porous domain and it goes to zero smoothly outside of it. This approach has been pursued, among others, by Angot *et al.* (1999) and Bruneau & Mortazavi (2008). Cimolin & Discacciati (2013) have shown that even if the penalization method is stable and easy to implement, the comparison of the solution against experimental data near the interface is not satisfactory.

Summing up, the interface conditions can be essentially classified into three classes: the first one involves pressure and velocities which are linked over the interface directly (continuity or jump); the second one involves them indirectly, linking the normal to the interface components of the stress tensor. The second class cannot be employed if the equation to be solved in the porous medium is Darcy's law. The
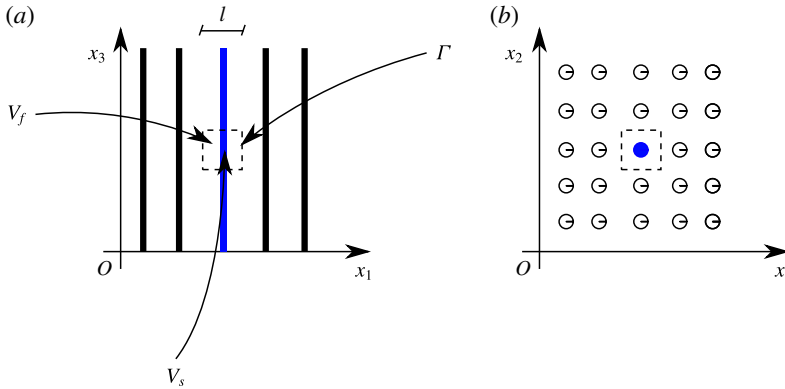
FIGURE 2. (Colour online) View of the particular porous medium studied in this work. The solution is assumed *V*-periodic, on the elementary cell defined by dashed lines.

third class includes all those methods which use a filter to go from the porous region to the fluid region; a drawback of this latter approach is that there is no general physical justification for the choice of the filter. Some authors (Breugem, Boersma & Uittenbogaard 2004; Jamet & Chandesris 2009) have proven that the variation of the permeability near the interface is not an intrinsic property of the porous medium, but depends on the properties of the flow.

In the first part of the present paper, using a homogenization technique, a strategy to develop models for flow through a bed of dense, rigid fibres is explained (figure 2). Particular attention is paid to the flow regime, so that two models are deduced: a classical one for Stokes' flows and an original one which accounts for inertial effects. For each regime two sets of equations apply: one microscopic and one macroscopic. Solving both sets of equations, a complete description of the flow inside the porous medium is obtained. In the second part of the work the models are validated on the basis of numerical simulations which solve for the fluid flow through a real, porous geometry (constituted by fibres), and against experiments of turbulent flows through a canopy (Ghisalberti & Nepf 2004, 2006, 2009).

2. Multiple scale analysis

Let us focus, for the moment, only on the flow inside a porous medium, neglecting the interface with the pure fluid domain. We consider an unbounded, rigid, porous medium saturated by an incompressible Newtonian fluid of constant density ρ and dynamic viscosity μ. The velocity and pressure fields in the fluid domain V_f are ruled by the incompressible Navier–Stokes equations:

$$\frac{\partial u_i}{\partial x_i} = 0, \tag{2.1}$$

$$Re\frac{\partial u_i}{\partial t} + Re u_j \frac{\partial u_i}{\partial x_j} = -\frac{1}{\epsilon}\frac{\partial p}{\partial x_i} + \nabla^2 u_i, \tag{2.2}$$

with $u_i = 0$ on the solid–fluid interface Γ. The equations above have been rendered dimensionless assuming that the global pressure gradient is balanced by the local viscous term, i.e.

$$O\left(\frac{\Delta P}{L}\right) \sim O\left(\frac{\mu U}{l^2}\right), \tag{2.3}$$

which defines the pressure scale, and time is normalized by l/U, where l is a microscale length which represents a characteristic dimension of the solid inclusions and L is a macroscale associated to the global pressure gradient ΔP. In this way the ordering symbol ϵ is defined as

$$\epsilon = \frac{l}{L} \ll 1, \tag{2.4}$$

and the Reynolds number, based on microscale length l and reference velocity U, is $Re = Ul/\nu$, with $\nu = \mu/\rho$ the kinematic viscosity.

2.1. *The expansion in ϵ*

Since the structure of the medium defines two characteristic scales, we need to introduce the fast (microscopic) and slow (macroscopic) variables x and $x' = \epsilon x$ with the subsequent change in the derivative:

$$\frac{\partial}{\partial x_i} \rightarrow \frac{\partial}{\partial x_i} + \epsilon \frac{\partial}{\partial x_i'}, \tag{2.5}$$

plus the expansion:

$$f = f^{(0)} + \epsilon f^{(1)} + \cdots, \tag{2.6}$$

where f represents a generic variable of the unknown field, function of (x, x', t). This choice highlights the dual nature of the problem, i.e. the partition between microscopic and macroscopic aspects of the problem connected by the fundamental concept of averaging (cf. the next section). Once we have substituted the expansion (2.6) into the governing equations, grouping each term in orders of ϵ and considering only those of order 0 and 1, we obtain the following equations defined over V_f:

$$\frac{\partial u_i^{(0)}}{\partial x_i} = 0, \tag{2.7}$$

$$\frac{\partial u_i^{(1)}}{\partial x_i} + \frac{\partial u_i^{(0)}}{\partial x_i'} = 0, \tag{2.8}$$

$$0 = -\frac{\partial p^{(0)}}{\partial x_i}, \tag{2.9}$$

$$Re \left(\frac{\partial u_i^{(0)}}{\partial t} + u_j^{(0)} \frac{\partial u_i^{(0)}}{\partial x_j} \right) = -\frac{\partial p^{(1)}}{\partial x_i} - \frac{\partial p^{(0)}}{\partial x_i'} + \frac{\partial^2 u_i^{(0)}}{\partial x_j \partial x_j}. \tag{2.10}$$

Equation (2.9) yields $p^{(0)} = p^{(0)}(x', t)$, i.e. the leading-order term of the pressure varies only over the macroscale (and time). Equation (2.10) contains the inertial terms which may, or may not, be negligible depending on the order of magnitude of the microscopic Reynolds number, Re.

2.2. *$Re = O(\epsilon)$*

If the Reynolds number is of order ϵ, the left-hand side of (2.10) goes to higher order, so that, following Mei & Vernescu (2010), the solution can be written formally as

$$u_i^{(0)} = -K_{ij} \frac{\partial p^{(0)}}{\partial x_j'}, \quad p^{(1)} = -A_j \frac{\partial p^{(0)}}{\partial x_j'} + p_0^{(1)}(x', t), \tag{2.11a,b}$$

where K_{ij} is a tensor, A_j is a vector and $p_0^{(1)}$ is an integration constant (with respect to the integration variable $\boldsymbol{x}$). Substituting (2.11) into (2.7) and (2.10) and simplifying, it follows that the coefficients should satisfy the relations:

$$\frac{\partial K_{ij}}{\partial x_i} = 0, \quad -\frac{\partial A_j}{\partial x_i} + \nabla^2 K_{ij} = -\delta_{ij}; \qquad (2.12a,b)$$

this is a forced Stokes problem with the unknowns K_{ij} and A_j for $i, j = 1, 2, 3$ (in principle a system of 12 equations and 12 unknowns) with boundary condition

$$K_{ij} = 0 \quad \text{on } \Gamma, \qquad (2.13)$$

plus periodicity over V for K_{ij} and A_j. We note that the solution of (2.12), (2.13) depends only on the microscopic spatial scale. Moreover, to ensure uniqueness of the solution we can impose

$$\langle A_j \rangle = 0, \qquad (2.14)$$

for each j, where the volume average over a unit cell $\langle \cdot \rangle$ is defined by:

$$\langle f \rangle := \frac{1}{V} \int_{V_f} f \, dV. \qquad (2.15)$$

By taking the volume average of (2.11), noting that $p^{(0)}$ and $p_0^{(1)}$ do not depend on $\boldsymbol{x}$ and using (2.14), we obtain

$$\langle u_i^{(0)} \rangle = -\mathscr{K}_{ij} \frac{\partial p^{(0)}}{\partial x_j'}, \quad \text{with } \mathscr{K}_{ij} = \langle K_{ij} \rangle, \qquad (2.16)$$

$$\langle p^{(1)} \rangle = \vartheta p_0^{(1)}, \quad \text{with } \vartheta = \frac{V_f}{V}, \qquad (2.17)$$

where $\mathscr{K}_{ij}$ is the dimensionless permeability tensor, the dimensional counterpart of which scales like l^2, and ϑ the porosity. Equation (2.16) is Darcy's law, which is a first-order approximation of the Navier–Stokes equations in ϵ. We thus have a macroscopic problem formed by the volume average of (2.8) which, after application of the spatial averaging theorem (Mei & Vernescu 2010), leads to

$$\frac{\partial \langle u_i^{(0)} \rangle}{\partial x_i'} = 0, \qquad (2.18)$$

plus (2.16), in which the tensor $\mathscr{K}_{ij}$, calculated through (2.12), appears. Darcy's law is based on the assumption that $Re = O(\epsilon)$. In view of the practical developments of this work, we now want to understand how to treat the problem when Re is not infinitesimal. One obvious extension consists in taking higher-order terms in the expansion (2.6), as done in Mei & Vernescu (2010). This leads to Darcy–Forchheimer's equation, valid in the range $\epsilon < Re < 1$. In §2.3 an alternative is proposed.
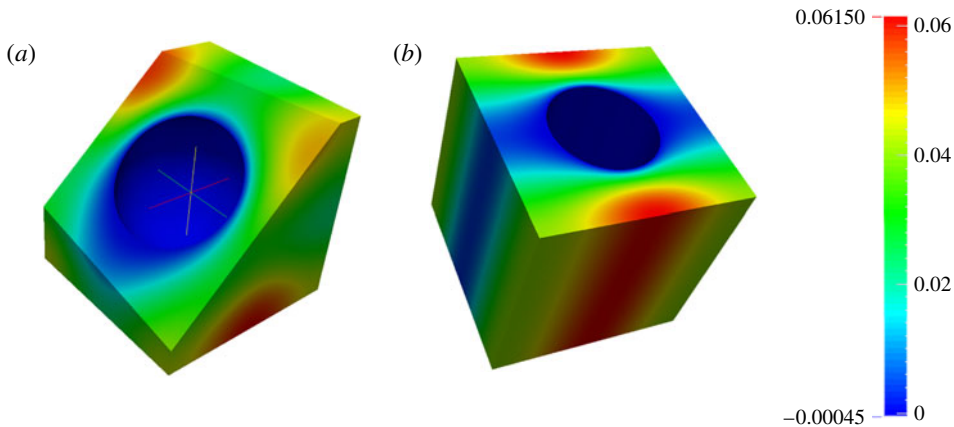
FIGURE 3. (Colour online) Isocontours of K_{11} in the microscopic domain for the case of porous media made by packed spheres (*a*) and cylindrical fibres (*b*).

2.2.1. *Microscopic simulations*

In order to solve (2.16), we first need to calculate the permeability tensor over the normalized domain shown in figure 3. For both cases $Re = O(\epsilon)$ and $Re = O(1)$ an opensource solver based on OpenFOAM (www.openfoam.com) is used. A time-marching solver is employed to reach a steady solution. The differential operators are discretized using the finite volume method and the Gauss scheme is employed to express the divergence, gradient and Laplacian operators; we have verified that the results reported here are grid converged.

We have first computed the case of an isotropic porous medium formed by packed spheres; our results for $\hat{\mathscr{K}} = \langle K \rangle$ match perfectly those obtained by Zick & Homsy (1982) for varying values of the porosity ϑ (cf. figure 4). The values of Zick & Homsy (1982) are Stokes flow results, obtained through the technique of integral equations, for different packings of uniform spheres. The much-quoted Kozeny–Carman empirical formula (Carman 1939):

$$\hat{\mathscr{K}} = \frac{1}{5} \left(\frac{V_s}{|\Gamma|} \right)^2 \frac{\vartheta^3}{(1 - \vartheta)^2}, \tag{2.19}$$

is close to the theoretical findings only for ϑ around 0.5; in the formula, $|\Gamma|$ is the interface area and V_s the solid volume. A better fit through the data, to represent the isotropic permeability as a function of the porosity, is given by:

$$\hat{\mathscr{K}} = \frac{1}{5} \left(\frac{V_s}{|\Gamma|} \right)^2 \frac{\vartheta^{5/2}}{(1 - \vartheta)^{47/30}} \tag{2.20}$$

(dashed red line in figure 4), valid in the range $0.476 < \vartheta < 1$.

The second step is to find the permeability of our particular porous medium and its orthotropic structure reduces to two the components of the tensor to be computed: K_{11} and K_{33} represent the longitudinal and transversal components of the permeability, respectively. Once K_{11} and K_{33} are found, we have a pointwise solution inside the elementary cell V; as before, we carry out the weighted integral of K_{ij} over its microscopic domain, as by (2.15), to obtain $\mathscr{K}_{11}$ and $\mathscr{K}_{33}$. The results are displayed
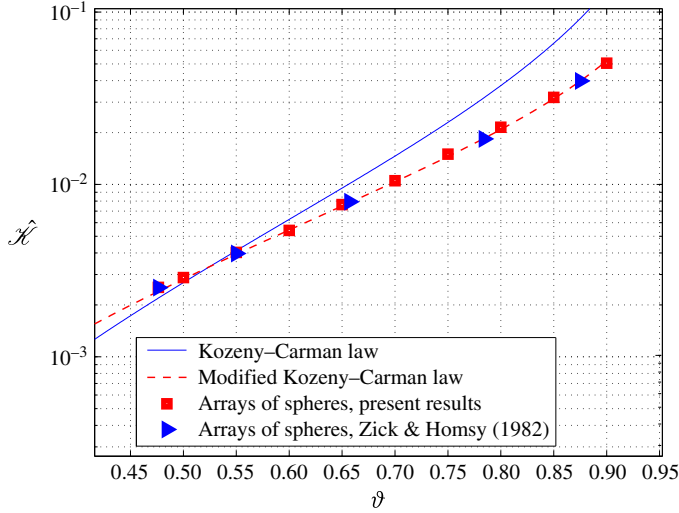
FIGURE 4. (Colour online) Permeability versus porosity for regular arrays of spheres: homogenization theory ($\square$ (red)), empirical law of Kozeny–Carman (—— (blue)), theoretical results by Zick & Homsy (1982) ($\triangleright$ (blue)).

in figure 5 against a set of theoretical and experimental data from the literature, with close agreement for ϑ ranging from 0.3 to 0.9. Thanks to figures 4 and 5, one can conclude that model (2.12) reproduces well the values of the permeability both in isotropic and anisotropic cases. The homogenization technique is thus suitable from a microscopic point of view and for low-*Re* flows, despite the fact that the permeability components vary over a wide range of values, from $O(10^{-4})$ to $O(10^{-1})$ depending on the porosity, an indication of the fact that l^2 is the proper scale for the permeability only at large porosities ϑ's. This is confirmed by numerical solutions of (2.12), which yield $\mathcal{K}_{ij} \to \delta_{ij}$ for $\vartheta \to 1$.

2.3. $Re = O(1)$

When *Re* is not small, (2.10) remains unaltered. We consider a steady solution of (2.10) through a Oseen approximation of the advective term, i.e. we assume that

$$u_j^{(0)} \frac{\partial u_i^{(0)}}{\partial x_j} \approx \overline{U}_j \frac{\partial u_i^{(0)}}{\partial x_j}, \tag{2.21}$$

where $\overline{U}_j$ is the mean fluid velocity vector through the medium defined via a spatial average:

$$\overline{U}_j := \frac{1}{V_{Tot}} \int_{V_{Tot}} \langle u_j^{(0)} \rangle \, \mathrm{d}V, \tag{2.22}$$

with V_{Tot} the whole macroscopic volume of the porous medium (fluid plus solid). We can also define the mean fluid velocity vector through the pores as $v^p = \overline{U}/\vartheta$ and the pore Reynolds number, $Re_p = U_p l/\nu$, where U_p is the scale of the pore velocity v^p.

The Oseen approximation has been proposed for cases with $Re \gg 1$ by Gustafsson & Protas (2013), with satisfactory results. We adopt it here in order to maintain a linear
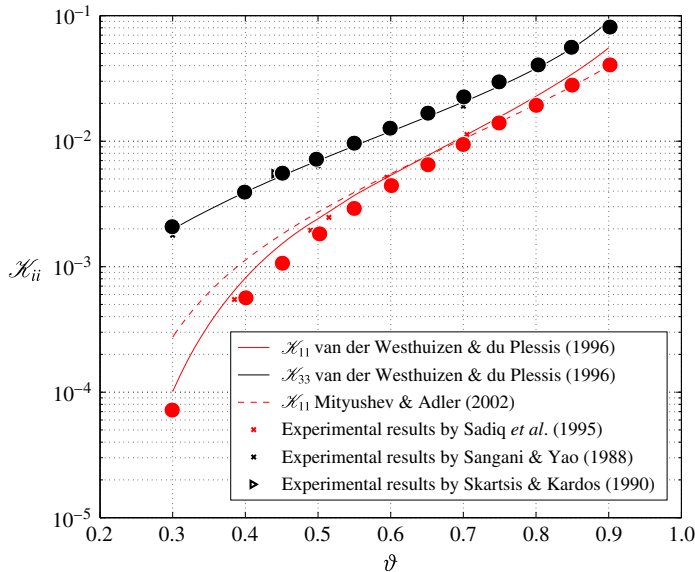
FIGURE 5. (Colour online) Components of the permeability tensor versus porosity for regular arrays of cylinders. The present results are represented by bullets, red for $\mathscr{K}_{11} = \mathscr{K}_{22}$, black for $\mathscr{K}_{33}$.

problem yielding (2.16). The choice of a global estimate of the velocity $\overline{U}$, defined via (2.22), is important to establish a two-way link between the microscopic and the macroscopic set of equations. Hence, we can write the solution of the new linearized equations as in (2.11) and search for K_{ij} and A_j which satisfy

$$\frac{\partial K_{ij}}{\partial x_i} = 0, \quad -\vartheta Re_p v^p_l \frac{\partial K_{ij}}{\partial x_l} = \frac{\partial A_j}{\partial x_i} - \frac{\partial^2 K_{ij}}{\partial x_g^2} - \delta_{ij}, \quad (2.23a,b)$$

with the same boundary conditions as those used in problem (2.12). For the definition of $\boldsymbol{v}^p$ to make sense, we need to implement an iterative method, as we will explain in § 4.1. Finally, Darcy's law has the same form as the canonical one (2.16), but the permeability tensor arises from iterating between the macroscopic equation (2.16) and the system (2.23) valid at the microscopic level. Thus, the permeability in this case is no longer a simple material property, but depends on the Reynolds number and the orientation of the velocity vector; it has been termed apparent permeability by Edwards *et al.* (1990). In the simple case in which the fluid has a single main direction of motion x_1, with constant pore velocity, i.e. $\boldsymbol{v}^p = (1, 0, 0)$, (2.23) becomes:

$$\frac{\partial K_{ij}}{\partial x_i} = 0, \quad -\vartheta Re_p \frac{\partial K_{ij}}{\partial x_1} = \frac{\partial A_j}{\partial x_i} - \frac{\partial^2 K_{ij}}{\partial x_g^2} - \delta_{ij}. \quad (2.24a,b)$$

2.3.1. *Effect of Re_p on the apparent permeability*

The procedure briefly outlined in § 2.3 for calculating the apparent permeability at varying values of the pore Reynolds number is here validated against simulations of the Navier–Stokes equations for the flow through regular arrays of cylinders
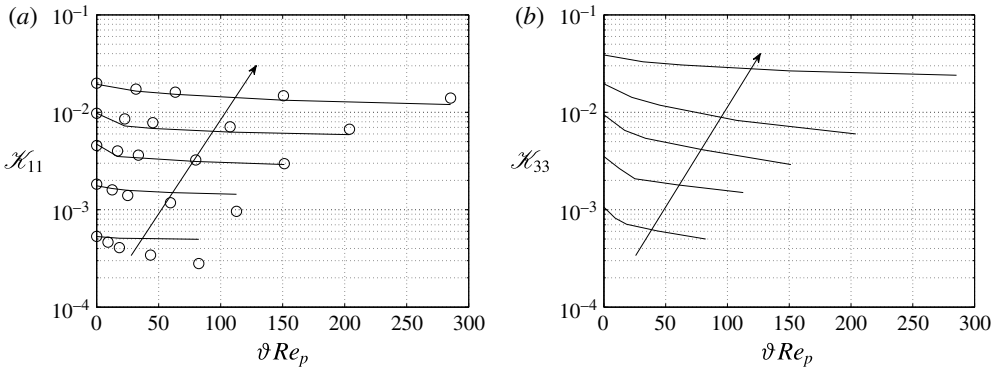
FIGURE 6. Components of the apparent permeability as a function of the pore Reynolds number. The arrows point in the direction of increasing values of ϑ, from $\vartheta = 0.4$ to 0.8 in intervals of 0.1. Symbols in (*a*) refer to the results by Edwards *et al.* (1990).

arranged in a square lattice. The reference simulations by Edwards *et al.* (1990) are two-dimensional (as such they furnish only the value of $\mathcal{K}_{11}$), and are carried out with a finite element solver for Re_p up to approximately 400 and porosities ϑ in the range 0.4–0.8. The comparison between our solutions of (2.24) and the reference values of $\mathcal{K}_{11}$ is shown in figure 6, as a function of the Reynolds number and the porosity of the medium, together with our solutions for $\mathcal{K}_{33}$. The Oseen-based approximations of the first component of the permeability tensor match satisfactorily the reference values, providing confidence in the model developed, particularly for larger porosities.

3. Interface conditions

The theory described thus far is based on the spatial homogeneity of the porous medium and is not valid, in general, when homogeneity is broken by, e.g., the presence of an interface with a different medium. We must thus pay particular attention to the conditions to be imposed to transfer information from the pure fluid region (denoted in the following by F with the corresponding unknown fields $\cdot|_F$) to the porous medium (denoted by P with the corresponding unknown fields $\cdot|_P$) and *vice versa*: near the actual physical interface a more or less thin buffer layer exists where a matching must be enforced.

Several interface conditions are present in the literature and a recent review can be found in Carraro *et al.* (2013). We have tested many of them comparatively; all conditions contain a certain degree of arbitrariness and require the *a posteriori* calibration of one or more parameters. We should also highlight the fact that a 'double' set of conditions is needed, one that links the fluid equations to Darcy's law, and the other which takes the results computed in P and transforms them into suitable interface conditions for the Navier–Stokes solver. Among the different strategies that we have tested, we outline and compare three of them.

A. The first approach consists in solving Darcy's equation in the porous region and imposing

$$p^{(0)}\big|_P = p\big|_F + \text{constant}, \tag{3.1}$$

at a fictitious interface positioned a small distance δ, which we call the penetration depth, below the physical interface, in order to transfer information from the fluid

region to the porous region. The presence of the constant term has no influence on the solution of Darcy's equation, since the pressure is always specified (both in P and F) up to an arbitrary constant; the constant is however maintained, at least formally, in (3.1) to highlight the fact that pressure may be discontinuous when crossing the interface. More specifically, a pressure jump has been predicted by Marciniak-Czochra & Mikelić (2012) and Carraro *et al.* (2013) when the porous medium is anisotropic or in the presence of flow inertia (see also Sahraoui & Kaviany 1992), and it varies along the interface direction. On the other hand, continuity of pressure across the interface, up to the order of the pore size, was advocated by Ene & Sánchez-Palencia (1975). We will come back to the pressure jump condition in §4.6.

To have adequate conditions for the Navier–Stokes equation, we use

$$u_i|_F = \langle u_i^{(0)} \rangle \Big|_P, \tag{3.2}$$

applied at the same fictitious interface as above. Here $u_i|_F$ is not averaged because it is the effective velocity, computed over a grid in which each point corresponds to a microscopic cell. Enforcing the continuity of both pressure and velocity below the real interface has been proposed and tested by Le Bars & Worster (2006), with the scope of accounting for inertia within the porous layer in the immediate vicinity of the fluid domain. Le Bars & Worster (2006) have shown that this is essentially equivalent to the interface condition of Beavers & Joseph (1967), which is applied at the physical interface, and have estimated the distance δ to vary as

$$\delta = c\sqrt{\frac{\mathscr{K}}{\vartheta}}, \tag{3.3}$$

where $\mathscr{K}$ represents the permeability (in their case a scalar since the medium is isotropic) and c is a constant to be determined ($c = 1$ in their work). By enforcing the conditions at δ, we are sufficiently far from the interface for the periodicity assumption of homogenization theory to remain tenable.

B. The second approach (e.g. Kaviany 1995) consists in modifying Darcy's equation adding a viscous term through which we can impose continuity of the velocity and the tangential and normal components of the stress tensor over the interface. We note that Brinkman's equation can be obtained from homogenization theory (Mei & Vernescu 2010), adopting slightly different normalizations of the starting equations on the assumption that the fibres are sufficiently sparse. The resulting equation, in terms of the scales used in the multiple scale theory, is

$$\langle u_i^{(0)} \rangle = -\mathscr{K}_{ij} \frac{\partial p^{(0)}}{\partial x_j'} + \mathscr{K}_{ij} \epsilon^2 \frac{\mu_e}{\mu} \frac{\partial^2 \langle u_j^{(0)} \rangle}{\partial x_k'^2}, \tag{3.4}$$

where μ_e is the (*a priori* unknown) effective viscosity of the homogenized medium. In order to match the results at the interface with the fluid region F, we should scale the pressure in Brinkman's equation with ρU^2, so that the newly normalized equation reads:

$$\langle u_i^{(0)} \rangle = -\mathscr{K}_{ij} \epsilon^2 Re_L \frac{\partial p}{\partial x_j} + \mathscr{K}_{ij} \epsilon^2 \frac{\mu_e}{\mu} \frac{\partial^2 \langle u_j^{(0)} \rangle}{\partial x_k^2}, \tag{3.5}$$

with Re_L the macroscopic Reynolds number, $Re_L = Re/\epsilon$, with the primes ′ now omitted from the name of the macroscale variable, x_i'. We also omit the superscript

(0) from the variable p in the porous domain. If μ_e were available we could impose the following conditions at the fluid–porous interface:

$$\left.(\sigma_{ij}n_j)n_i\right|_F = \left.(\sigma_{ij}n_j)n_i\right|_P \quad \text{and} \quad \left.(\sigma_{ij}n_j)t_i\right|_F = \left.(\sigma_{ij}n_j)t_i\right|_P \qquad (3.6a,b)$$

to transfer data from the fluid domain to the porous medium P ruled by Brinkman's equation, plus (3.2) to go from the porous domain to the fluid domain. In (3.6), σ_{ij} is the stress tensor, n_i and t_i are, respectively, the unit vectors normal and tangent to the interface. Such conditions can be written in the present case as

$$\left.\left(\frac{\partial u_1}{\partial x_3} + \frac{\partial u_3}{\partial x_1}\right)\right|_F = \frac{\mu_e}{\mu}\left.\left(\frac{\partial \langle u_1^{(0)}\rangle}{\partial x_3} + \frac{\partial \langle u_3^{(0)}\rangle}{\partial x_1}\right)\right|_P \qquad (3.7)$$

and

$$\left.\left(-p + \frac{2}{Re_L}\frac{\partial u_3}{\partial x_3}\right)\right|_F = \left.\left(-p + \frac{\mu_e}{\mu}\frac{2}{Re_L}\frac{\partial \langle u_3^{(0)}\rangle}{\partial x_3}\right)\right|_P. \qquad (3.8)$$

We note that the stress from the pure fluid region F is transmitted to the homogenized region P, and is distributed to both the inclusions (the fibres) and the fluid contained within them.

C. The third interface condition tested consists in applying the same strategy as in A with $\delta = 0$, i.e. the matching is enforced precisely at the physical interface, but the permeability components are driven smoothly to a large absolute value near the interface, through a filter which forces the permeability to vary rapidly over a distance of the order of ϵ. This strategy has been proposed by Chandesris & Jamet (2008) and Jamet & Chandesris (2009); in the present case the filter is taken directly from three-dimensional numerical simulation results with account of all individual fibres.

4. First validation case: laminar flow in a cavity

We first solve for the flow in a composite domain, in which there is both a pure fluid region and a porous region formed by densely packed rigid fibres: the choice of considering a lid-driven cavity, filled up to a certain height (each fibre is in length 0.33 times the side length of the square cavity) by the porous medium, as sketched in figure 7, allows us to analyse the orthotropic character of the medium. In fact, because of the non-negligible vertical velocity inside the porous region, we are able to quantify how much K_{33} affects the fluid flow and we can impose and compare different interface conditions. On the other hand, this case is more difficult than the classical pressure-driven channel flow with porous walls studied by many authors before.

The method used is classified as a domain decomposition method; it is an iterative method based on splitting interface conditions, which play the role of transmission conditions (cf. Quarteroni & Valli 1999), between the F and P regions. Searching for a steady solution we formalize the numerical procedure with the following steps:

(i) We solve for the two-dimensional NSE in the F-region, expressed in dimension-less form as:

$$\frac{\partial u_i}{\partial x_i} = 0, \qquad (4.1)$$

$$\frac{\partial u_i}{\partial t} + u_j\frac{\partial u_i}{\partial x_j} = -\frac{\partial p}{\partial x_i} + \frac{1}{Re_L}\nabla^2 u_i, \qquad (4.2)$$
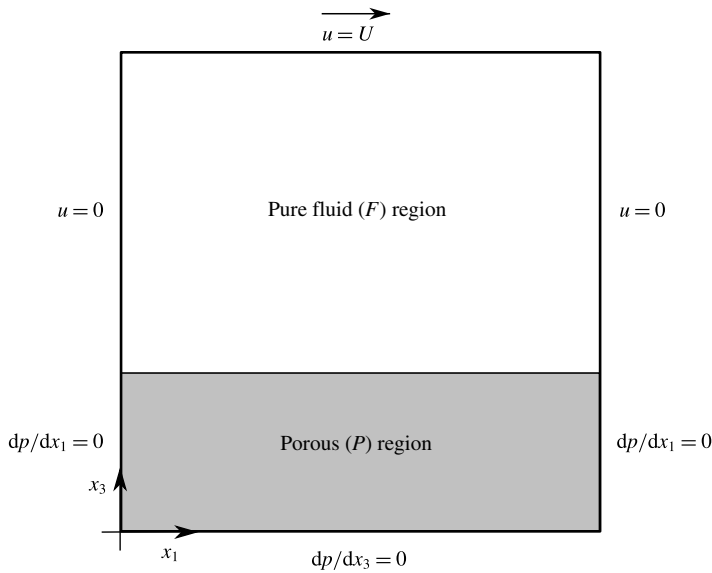
FIGURE 7. View of the macroscopic domain with the boundary conditions imposed when solving Darcy's equation in the *P*-region.

with initial interface condition $\boldsymbol{u} = 0$; Re_L is based on the characteristic dimension of the cavity (L) which can be identified with the macroscopic length of the homogenization technique, so that $Re_L = Re/\epsilon$. The solver developed and validated in Zampogna (2016) is based on the fractional step method, using fourth-order finite differences for the space discretization and a Crank–Nicolson scheme for the time advancement (Perot 1993).

(ii) We take the divergence of (2.16) and use (2.18) to have in the *P*-region:

$$\mathscr{K}_{11}\frac{\partial^2 p}{\partial x_1^2} + \mathscr{K}_{33}\frac{\partial^2 p}{\partial x_3^2} = 0, \qquad (4.3)$$

plus homogeneous Neumann conditions on the solid walls. At the interface the pressure is imposed (cf. (3.1)). If the Brinkman's model is considered instead, conditions (3.7) and (3.8) are used at the interface, together with no slip along the walls, to solve for the equations in the porous domain and find the pressure $p|_P$ and the velocity components $(\langle u_1^{(0)} \rangle, \langle u_3^{(0)} \rangle)$.

(iii) When using Darcy's model we still need to compute the velocity in the porous medium, using (3.5) with μ_e set to zero. For either models the final step of the iteration procedure consists in enforcing condition (3.2) at the interface for the subsequent solution in the *F*-region.

4.1. *Double interactions for the $Re = O(1)$ case*

The scheme of the $Re = O(\varepsilon)$ case remains unchanged also when $Re = O(1)$, except for one point. In this case the permeability tensor cannot be computed before starting the macroscopic simulation but must be computed each time that Darcy's velocity is updated because K_{ij} depends directly on the magnitude and direction of the mean velocity inside the porous medium (cf. 2.23). A guessed value of K_{ij} is thus chosen
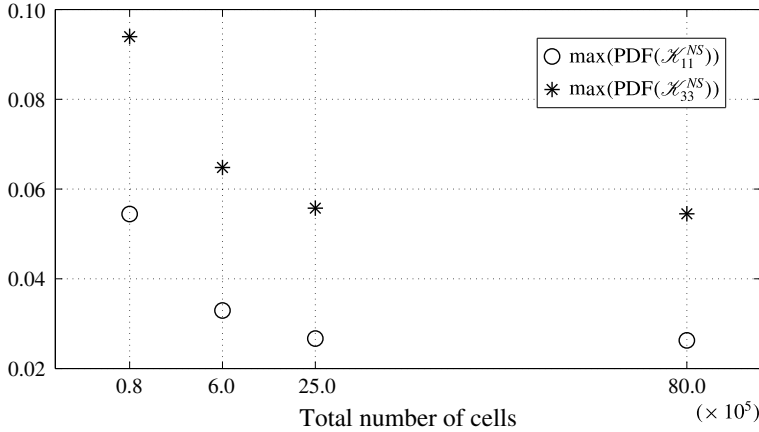
FIGURE 8. Spatial convergence study for the DNS in the case of $Re_L = 100$. The different grids are built with the software snappyHexMesh (http://www.openfoam.org/version2.3.0/snappyHexMesh.php).

to initialize the iterative procedure and a reasonable choice is to use the permeability of the Stokes flow case. After each solution in the *P*-region, the mean velocity components are computed with (2.22) and used to estimate the permeability for the successive time step.

4.2. *Direct numerical simulations*

In order to compare the different interface conditions and assess which of them fits the problem analysed in this work, three-dimensional direct numerical simulations (DNS) of the incompressible NSE in the real geometry, accounting for all fibres (50 for the simulations presented here, so that $\epsilon = 0.02$), are performed with OpenFOAM. Also in this case all the operators (divergence, gradient and Laplacian) are discretized using the finite volume method, with the Gauss linear scheme. A Crank–Nicolson scheme is used to march in time.

In the transverse direction (x_2) the size of the domain is taken equal to ϵ (in dimensionless terms) and periodic boundary conditions are enforced. The numerical mesh needed to have grid-converged solutions is formed by over 8 million cells; figure 8 provides an example of a convergence test for a measure (the PDF of the permeability components) introduced further in (§ 4.3).

An example of a DNS result (for $Re = 100$) is shown in figure 9, where a slice of the steady converged solution at $x_3 = 0.25$ (thus within the porous medium) is shown, through isocontours of the first velocity component, near the solid boundaries and around $x_1 = 0.5$. The figure also shows a cut through the numerical grid.

With the results from the DNS we can:

(i) evaluate the components of the permeability tensor and verify the results of homogenization theory;
(ii) test the different interface conditions and, for example, calibrate the constant *c* in the definition of δ (3.3);
(iii) validate the unknown fields at a macroscopic level, verifying the appropriateness of the homogenized equations.
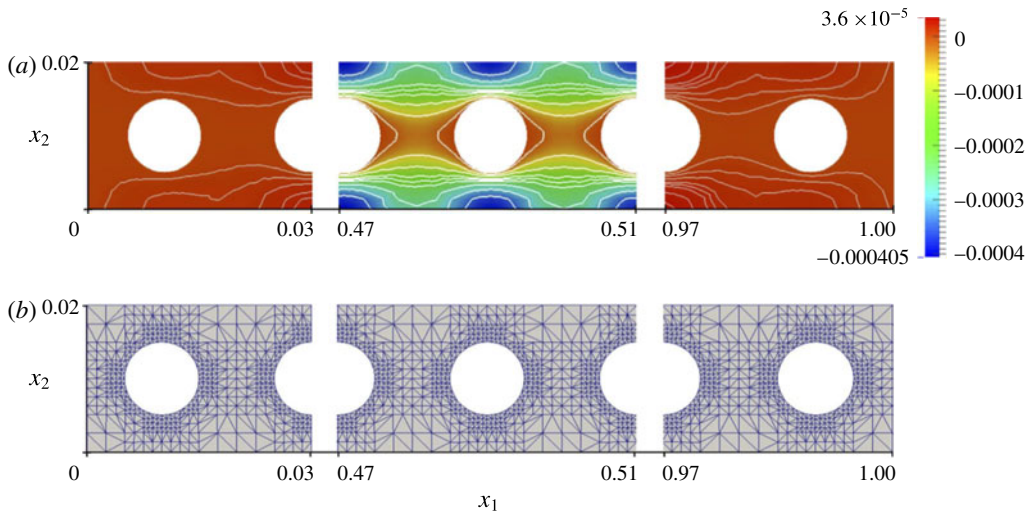
FIGURE 9. (Colour online) Zoom of the macroscopic domain of the DNS inside the porous medium with $\vartheta = 0.8$. Slice of the cavity at $x_3 = 0.25$. Only few cylinders (out of 50) are shown inside and at the extremities of the cavity. The colours and the white curves in (*a*) represent the x_1-component of the velocity field and its isocontours. In (*b*) a cut through the grid is shown.

To compare the DNS results with the two-dimensional simulations described in the previous section we must extract in a proper way the averaged values of the fields: the whole domain is thus decomposed into elementary cubic cells of size ϵ^3 and all fields are averaged over each microcell using the definition (2.15); in this way two-dimensional fields are obtained from the DNS results and, in particular, we have a sampling of the solution in the porous medium (in the case of a layer of N filaments of height 0.33 we have a Cartesian grid, with velocity components and pressure centred in the cell, composed by $0.33\,N^2$ elements in P). Using the grid built, the pressure gradient is computed with fourth-order finite differences. In the internal region of the porous medium, assuming that Darcy's approximation is valid (i.e. $\langle u^{DNS} \rangle = \langle u^{(0)} \rangle$ and $\langle p^{DNS} \rangle = p^{(0)}$), $\mathcal{K}_{ij}$ is computed using (2.16), using the same scalings which have led to (3.5). Finally, we need to account for the influence of the boundary layers at the solid walls and at the interface, and for the presence of isolated regions in which the pressure gradient becomes negligibly small; thus, the values of $\mathcal{K}_{ij}^{DNS}$ (superscript *DNS* is used to indicate that the value has been estimated on the basis of the full simulations) are evaluated on the basis of their probability density functions (PDF). To compute the PDF we divide the values of $\mathcal{K}_{ii}$ in a number of intervals such that each one of them has an extent equal to 10 % of the value of $\mathcal{K}_{ii}$ for which we find the maximum of the PDF.

4.3. *The components of the permeability tensor*

The complete simulations have been performed for Reynolds numbers Re_L varying from 1 to 1000, for fixed value of $\epsilon = 0.02$ and $\vartheta = 0.80$. The *a posteriori* treatment of the DNS results within the porous medium permits to extract the value of the permeability components over each elementary cubic cell, yielding the probability density functions displayed in figure 10.
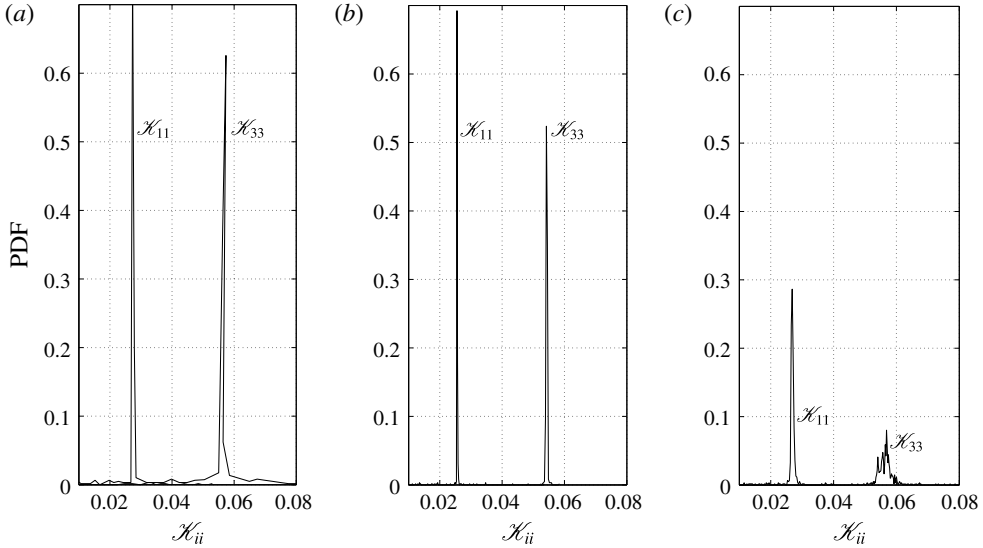
FIGURE 10. Probability density function of $\mathcal{K}_{11}$ and $\mathcal{K}_{33}$ for different values of Re_L. The apparent permeability is computed *a posteriori* applying Darcy's law to the averaged solution of the DNS. (*a*) $Re_L = 10$, (*b*) 100, (*c*) 1000.

It is immediately apparent that the PDF pinpoints sharply the values of $\mathcal{K}_{11}$ and $\mathcal{K}_{33}$ for Re_L up to 100, whereas for larger Re_L's the two components of the permeability display a broader variability. The peak values are nonetheless well defined and are reported in table 1, against corresponding results from the homogenization theory. The latter have been computed including inertial terms in the equations, with the same U_p found in the direct simulations of the full geometry. The values of the permeability components from the DNS are approximately 40 % larger than those calculated from the system (2.12), (2.13); in absolute terms, the difference is of order ϵ, consistent with the theory. We will see (figure 21) that something similar occurs also in another flow case, under turbulent conditions. In the narrow range of pore Reynolds number considered here, the full simulations do not allow us to extract a clear trend of how the permeability varies, whereas the theory indicates a slow decrease of both components with Re_p.

The disagreement between theory and direct simulations appears to be relatively mild, when seen in the scale of figure 6, but nonetheless deserves to be clarified, since it occurs also for flow cases ($Re_L = 1$) in which the motion of the fluid through the pores is clearly ruled by Stokes' equation. We believe that, on the one hand, the flow geometry plays a role here, since the two sidewalls constrain the fluid, forcing it to recirculate; a much better agreement would have been obtained had we considered a pressure-driven channel flow, as done by many authors (Le Bars & Worster 2006; Hill & Straughan 2008; Battiato 2012). On the other hand, we would expect a closer match between the DNS results and the theory had we pushed the asymptotic development to third order, modifying Darcy's equation with a Forchheimer term, as described by Mei & Vernescu (2010). This is indirectly supported by one direct simulation at $Re_L = 100$, conducted with 200 fibres (instead of 50) – for which the small parameter ϵ of the expansion is small (and equal to 0.005), for the same porosity coefficient $\vartheta = 0.80$ – which yields values of the apparent permeability closer to the theoretical ones in table 1.

Re_L	ϑU_p	ϑRe_p	$\mathcal{K}_{11}^{DNS}$	$\mathcal{K}_{33}^{DNS}$	$\mathcal{K}_{11}$	$\mathcal{K}_{33}$	d_1/ϵ	d_3/ϵ
1	4.40×10^{-5}	0.88×10^{-6}	2.62×10^{-2}	5.44×10^{-2}	1.89×10^{-2}	3.95×10^{-2}	3	1.5
10	4.50×10^{-5}	0.90×10^{-5}	2.66×10^{-2}	5.57×10^{-2}	1.89×10^{-2}	3.95×10^{-2}	2.7	1.5
100	7.01×10^{-5}	0.14×10^{-3}	2.63×10^{-2}	5.49×10^{-2}	1.89×10^{-2}	3.94×10^{-2}	2.5	1.5
1000	2.04×10^{-4}	0.41×10^{-2}	2.65×10^{-2}	5.63×10^{-2}	1.87×10^{-2}	3.93×10^{-2}	2.5	1.5

TABLE 1. Values of the permeability components from the DNS and homogenization theory. U_p represents the dimensionless mean pore velocity in the whole porous medium. Because of continuity, the mean pore velocity is oriented only along x_1. d_1 and d_3 are the distances from the interface starting from which $\mathcal{K}_{11}$ and $\mathcal{K}_{33}$ can be assumed constant when condition C is applied (cf. figure 16).
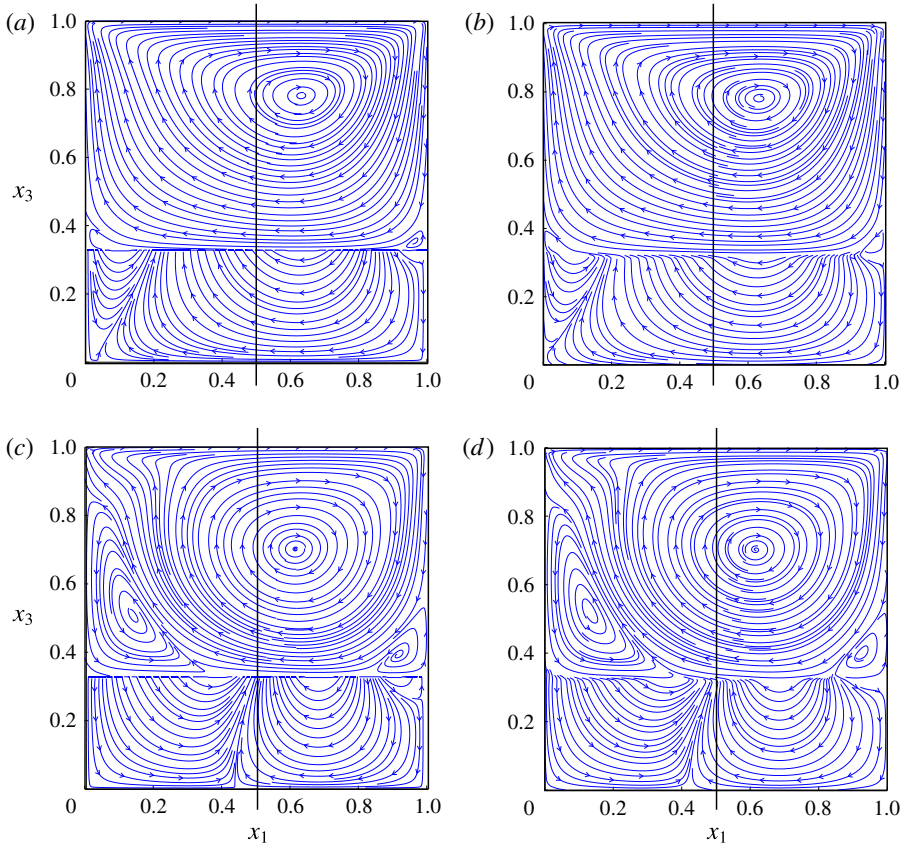
FIGURE 11. (Colour online) Streamlines in the composite domain. (*a*,*b*) Represent the solution for $Re_L = 100$; (*c*,*d*) display results for $Re_L = 1000$. In all cases the porosity is $\vartheta = 0.80$. (*a*,*c*) Show solutions of the homogenized model, (*b*,*d*) are the DNS results. Representative velocity profiles will be later displayed along the vertical line $x_1 = 0.5$.

In the following, the results from the three-dimensional numerical simulations will be compared to results from the coupled two-dimensional Navier–Stokes/Darcy equation, where in the latter model the values used for the apparent permeability are those of the direct numerical simulations.

4.4. *The macroscopic fields*

A representative comparison between the DNS results and those from the model system is displayed in figures 11 and 12 in terms of the streamlines of the flow and the pressure field, respectively. In the model system we have enforced interface conditions A (cf. §4), with $\delta = \epsilon/5$, i.e. we have used the penetration depth δ that, as we will show, yields the best agreement between the model and the direct simulations. The results are very close to one another and, in particular, the complex behaviour of the flow within the porous domain appears to be correctly captured by Darcy's equation (with a tensorial permeability). Also the pressure field of the homogenized model matches that of the DNS with the constant term of (3.1) appropriately chosen.

It is significant that the model problem requires a CPU time of the order of 30 minutes using one 2.0 GHz Intel®Xeon® processor and less than 2 Gb of RAM to
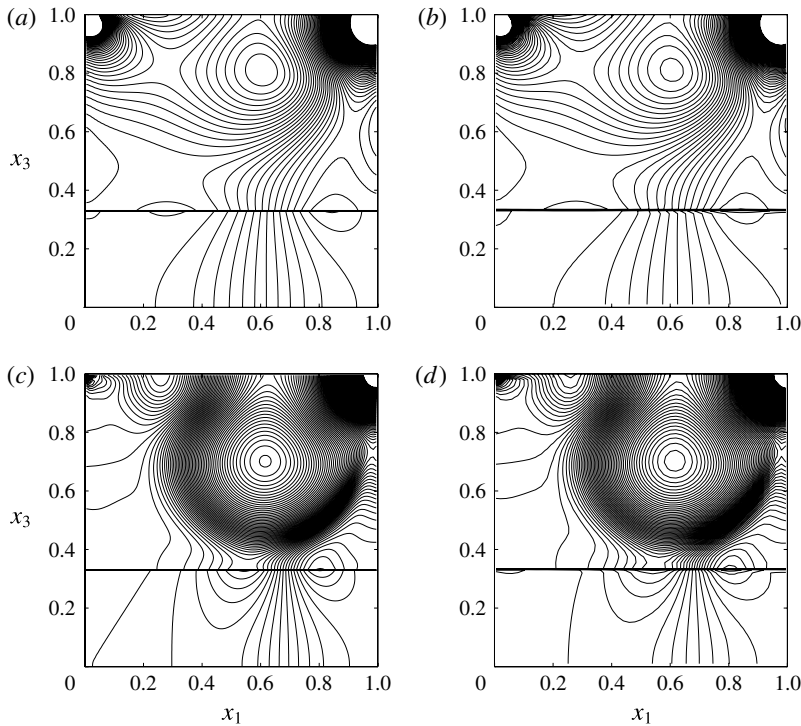
FIGURE 12. Isocontours of the pressure field in the composite domain. Panels (a,b) represent the solution for $Re_L = 100$; (c,d) display results for $Re_L = 1000$. In all cases the porosity is $\vartheta = 0.80$. Panels (a,c) are the solutions of the homogenized model, (b,d) are the DNS results.

reach convergence, whereas each DNS, on the same computer, needs a CPU time of over 500 h and more than 8 Gb of RAM, running in parallel on 16 processors. It is also noticeable that for different interface conditions the results are qualitatively similar, and all the model solutions look 'correct', with minor differences noticeable (corresponding images are not shown for reasons of space). This statement, however, justifies a closer look at the interface.

4.5. *Focus on the interface*

To assess the quality of the interface conditions we focus on $x_1 = 0.5$. The first condition (A of § 3) yields the results displayed in figure 13, for $Re_L = 100$. A value of δ between 0 and $\epsilon/5$ provides a good match with the DNS results in the F-region and at the interface, whereas increasing δ above $\epsilon/2$ yields values of both velocity components near the interface which progressively overestimate the 'true' values. Within the porous domain ($x_3 \leqslant 0.25$), the difference between the solutions computed for varying δ's and the DNS is negligible.

When Re_L is equal to 1000, an excellent agreement with the DNS results is achieved for $\delta = \epsilon/5$, as shown in figure 14. It is important to note that a poor choice of δ (e.g. $\delta \geqslant \epsilon$) degrades the solution also in the fluid region F, as figure 14 clearly demonstrates. As far as interface condition A is concerned, we observe an increase of the penetration depth, δ, with Re_p, as one would intuitively expect.
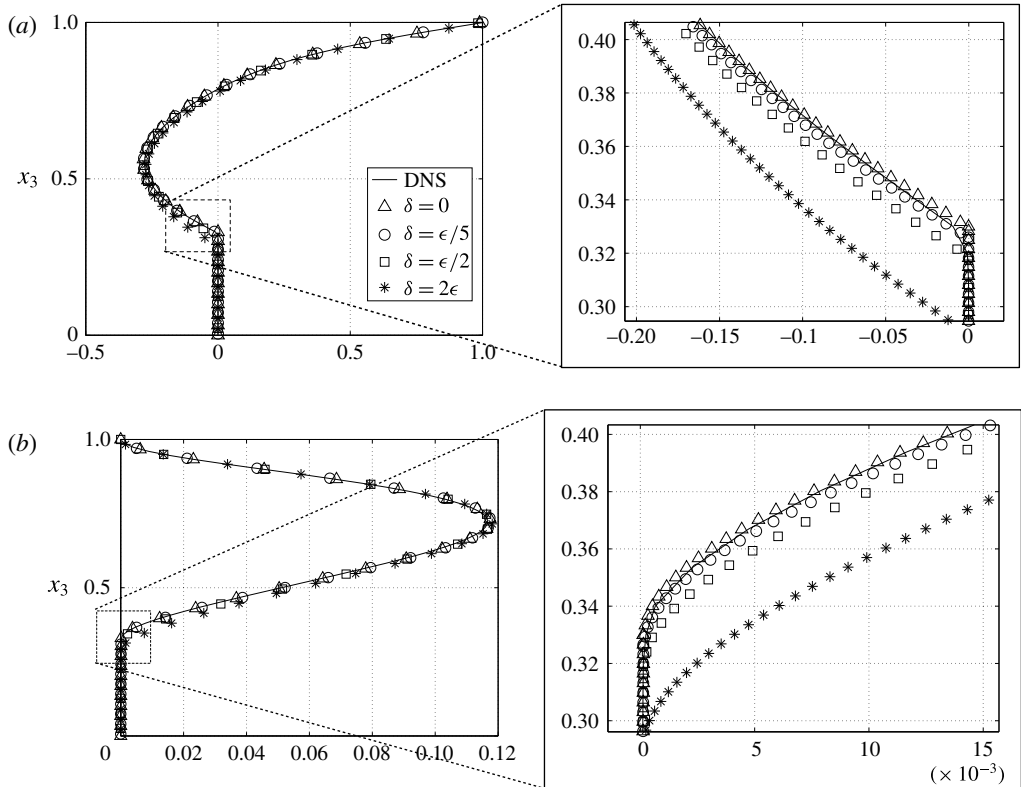
FIGURE 13. View of the macroscopic profile of u_1 and u_3 (lower panels) for $x_1 = 0.5$ (middle of the cavity) for the DNS and four choices of δ ($Re_L = 100$). Two zooms are highlighted at the interface. Interface strategy: A.

We now turn to interface condition B. Brinkman's equation has been discretized and directly matched to the Navier–Stokes results in the F-region; the velocity profiles obtained at $x_1 = 0.5$ are compared to the reference profiles in figure 15, for $Re_L = 100$ and different values of the effective viscosity. As μ_e approaches zero, the Darcy limit is recovered; the upper value of μ_e/μ considered is 30, close to that determined experimentally by Givler & Altobelli (1994). Furthermore, even the theoretical value, $\mu_e/\mu = (1 - \vartheta)^{-1} = 5$, deduced on the basis of volume averaging theory by Ochoa-Tapia & Whitaker (1995), has been tested. The immediate observation is that a value of the effective viscosity, which is either too large (30) or too small (0.3), degrades significantly the solution in the F-region, as a direct consequence of the poor estimation of the velocity in the proximity of the interface. Conversely, when μ_e is a few times larger than the dynamic viscosity of the fluid, i.e. it is close to the theoretical approximation, the solution appears to behave better when compared to the DNS, although close inspection of the fields within the porous region (not shown) show differences between the model solution and the 'exact' result which are larger than those found with interface strategy A. This negative aspect of Brinkman's model, coupled to the fact that the effective viscosity is not available *a priori*, is somehow tempered by the fact that Brinkman's equation has been used here in a system for which the fibres are not sufficiently sparse, as prescribed by Mei & Vernescu (2010). A similar conclusion on the poor performance of Brinkman's model
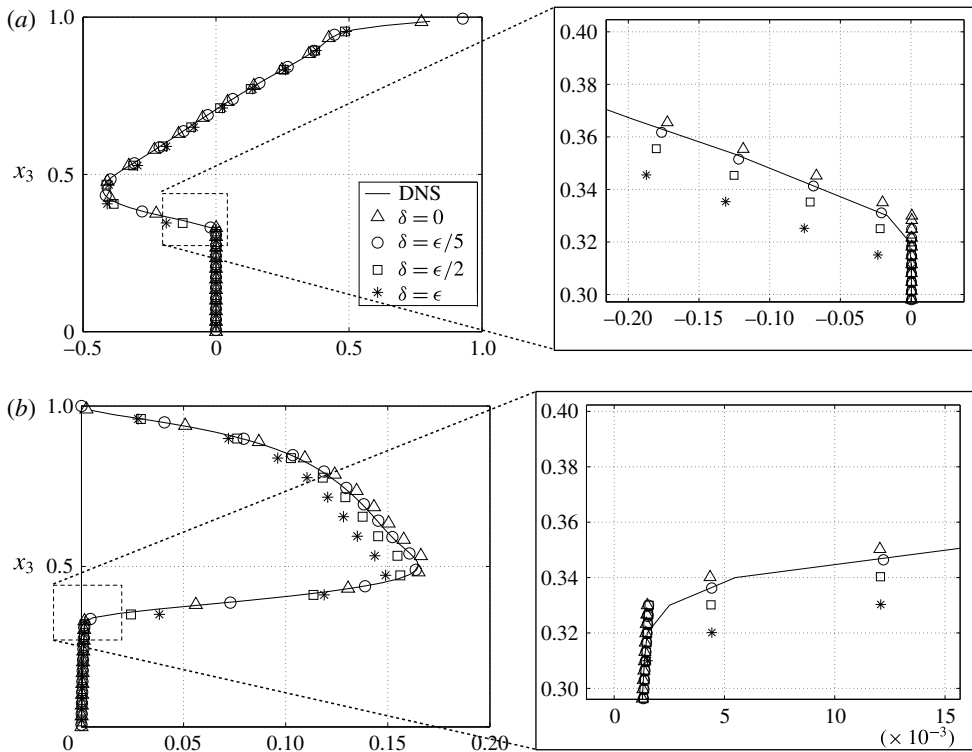
FIGURE 14. View of the macroscopic profile of u_1 and u_3 (lower panels) for $x_1 = 0.5$ for the DNS and four choices of δ ($Re_L = 1000$). Interface strategy: A.

in handling porous–fluid interfaces has also been reported by Sahraoui & Kaviany (1992), Kaviany (1995) and James & Davis (2001).

Results from the last interface condition (C) are displayed in figures 16 and 17; here the permeability varies as the macroscopic interface (at $x_3^{ITF} = 0.33$) is approached. Whereas this is physically reasonable, it is unknown how the permeability should be taken to vary. In this specific case we use the DNS results to define the shape of the filter to apply on $\mathcal{K}$. The permeability inside the porous medium is recovered using Darcy's law, as explained in the previous section. Here, we need a value of permeability for each x_3 in the porous zone. It is sampled for each x_1 in the cavity and then a mean value along the x_1 direction is extrapolated (solid and dotted lines of figure 16). It is clear that up to a distance $d = O(\epsilon)$ from the interface, the value of $\mathcal{K}_{ii}$ is constant; then it increases. In particular we observe that for the case $Re_L = 100$ shown in figure 16 the component $\mathcal{K}_{11}$ has $d_1 = (5/2)\epsilon$, while for $\mathcal{K}_{33}$ it is $d_3 = (3/2)\epsilon$. This seems to indicate that $\mathcal{K}_{ii}^{-1}$ is proportional to d_i; in table 1 this trend is further explored for varying Re_L's. The distance d_i ($i = 1, 3$) defines an interfacial layer whose thickness decreases slowly with the increase of the Reynolds number Re_L. In this it differs from the protrusion height δ of approach A. The agreement at the interface between the homogenized solution and the solution of the DNS is however not very good (cf. figure 17) and this is likely due to the fact that near the interface Darcy's law is inappropriate and a model which accounts for inertia is needed.
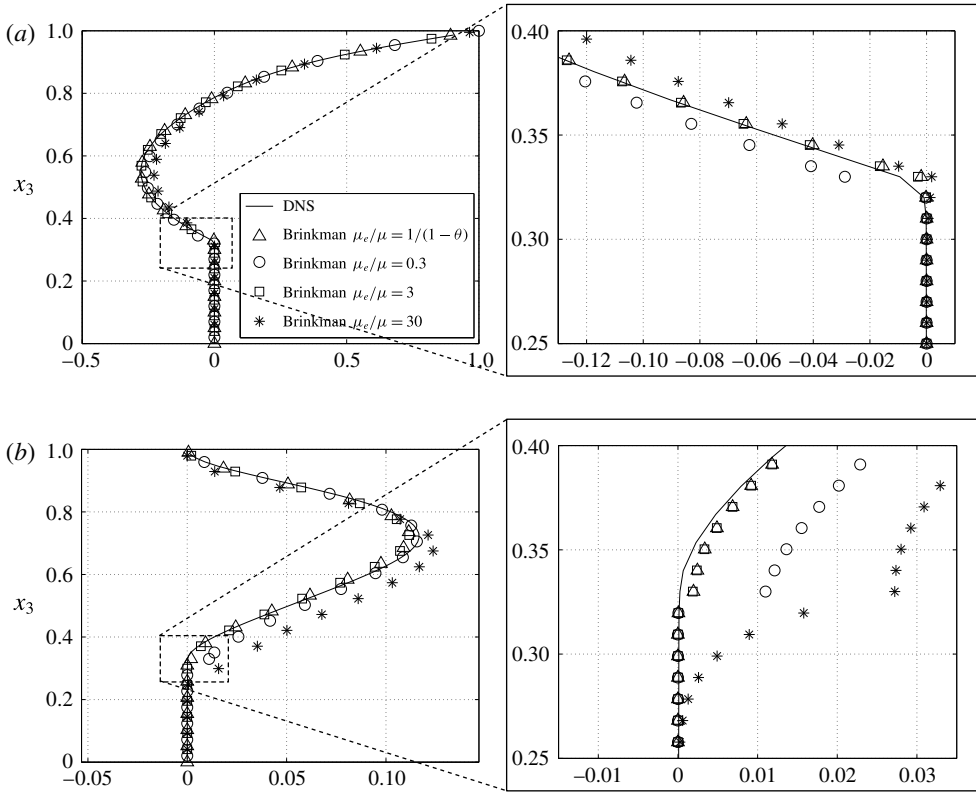
FIGURE 15. View of the macroscopic profile of u_1 and u_3 (lower panels) for $x_1 = 0.5$ and four choices of μ_e/μ ($Re_L = 100$). The images on the right highlight the degradation of the solution with increasing μ_e, in particular close to the interface. Interface strategy: B.
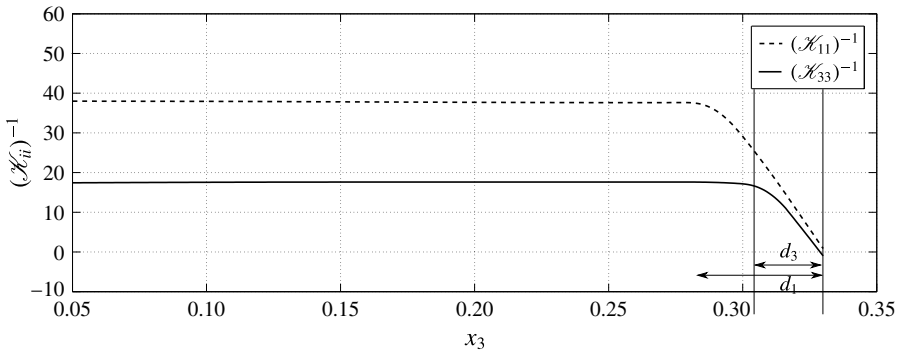

FIGURE 16. Inverse of the filtered permeability for the cases $Re_L = 100$. The two lines (dotted and solid) arise from the DNS and are x_1-averaged values; d_1 and d_3 are the lengths over which the components of permeability vary near the interface positioned in $x_3 = 0.33$.

4.6. *The pressure jump at the interface*

The availability of the DNS renders it possible to assess the presence of, and quantify, the pressure jump across the physical interface. Arguments for the existence
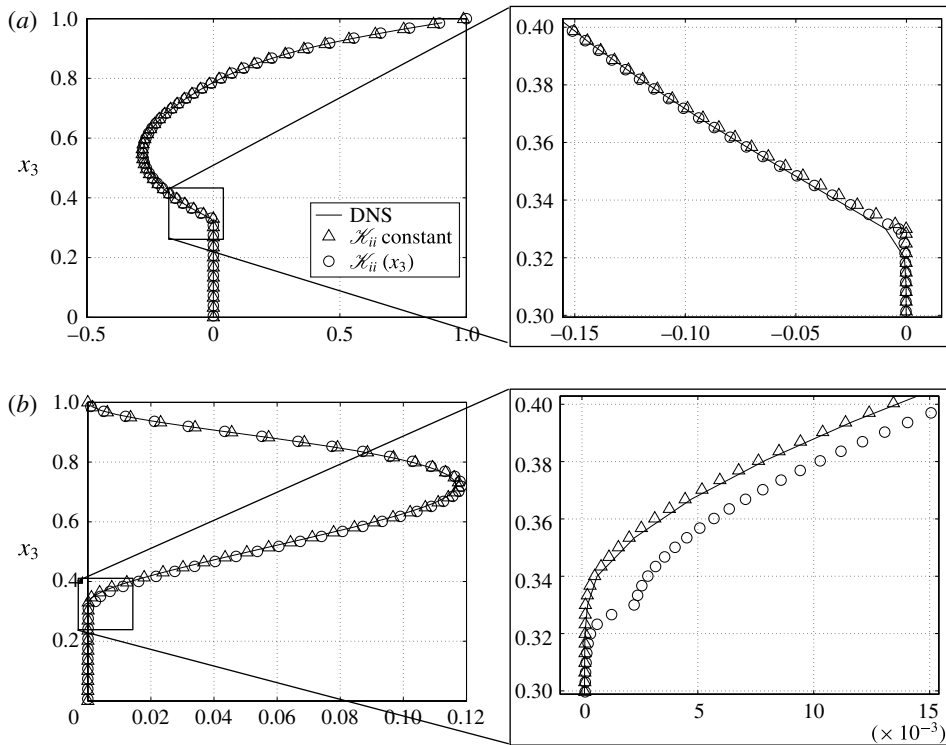
FIGURE 17. Macroscopic profile of u_1 and u_3 (lower panels) for $x_1 = 0.5$ computed using the filtered permeability shown in figure 16 ($Re_L = 100$) and compared to the case in which the permeability components are maintained constant throughout the porous zone. Two zooms over the interfacial zone are highlighted on the right. Interface strategy: C.

of a pressure jump have been put forward, using homogenization theory coupled with a boundary layer analysis near the interface, by Marciniak-Czochra & Mikelić (2012) for the Stokes flow over an anisotropic porous bed. Similarly, a pressure slip at the interface has been reported by Sahraoui & Kaviany (1992) in the presence of flow inertia; analytical arguments to quantify the pressure slip are given by Carraro *et al.* (2015) in the case of forced infiltration. The condition of Marciniak-Czochra & Mikelić (2012) in dimensionless form, reads:

$$-[p] = p_P(x_1, ITF^-) - p_F(x_1, ITF^+) = \frac{C}{Re_L} \frac{\partial u_1}{\partial x_3}(x_1, ITF), \qquad (4.4)$$

with the first term above representing the pressure jump across the interface, positioned at $x_3 = ITF$ and C a constant which depends only on the porous bed geometry. We have evaluated precisely this jump on the basis of the DNS, by averaging the microscopic data, both in F and P, over cubic unit cells of size ϵ^3. Thus, the pressure in the pure fluid is evaluated at $x_3 = ITF^+ = ITF + (\epsilon/2)$, and the average pressure in P is evaluated at $x_3 = ITF^- = ITF - (\epsilon/2)$. The left panel of figure 18 displays $|Re_L[p]|$ along the interface at the three values of Re_L considered; the right panel of the same figure reports a shear parameter defined as:

$$S = \frac{\partial u_1}{\partial x_3}(x_1, ITF) + \frac{\partial u_3}{\partial x_1}(x_1, ITF). \qquad (4.5)$$
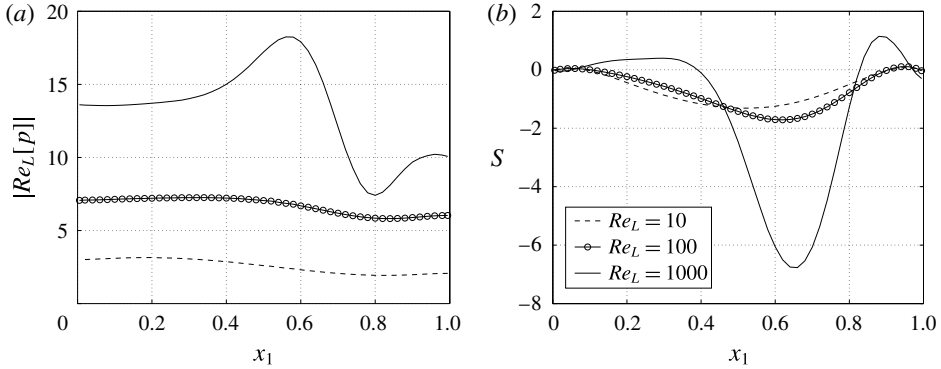
FIGURE 18. (*a*) Pressure jump across the interface at three values of the Reynolds number. (*b*) Shear parameters *S* at the interface. Both panels are based on DNS results.

In our simulations $(\partial u_3/\partial x_1)(x_1, ITF)$ at the interface is typically two orders of magnitude smaller than the $(\partial u_1/\partial x_3)(x_1, ITF)$ term, which thus dominates the parameter *S*. Comparison of the two panels makes it clear that, in the presence of inertia, a simple constant *C* cannot be found to satisfy the pressure jump condition, which is thus unsuited for use in the present case. Henceforth, although the pressure jump is present, condition (4.4) cannot be readily enforced.

5. Second validation case: turbulent canopy flow

In this section we want to demonstrate that the model formed by (2.16), (2.24) plus the equations in the pure fluid domain and the interface conditions are adequate also to simulate a turbulent canopy flow. This kind of flow has been widely studied in the past since it develops very often in nature (a recent review is provided by Nepf (2012)). Much literature (theoretical and experimental) is present to understand the mechanisms which induce the creation of a quasi-parallel mixing layer and the formation of honami and monami waves over canopies. Raupach, Finnigan & Brunet (1996) and Finnigan (2000) have classified the different structures which characterize the flow, on the basis of the geometrical properties of the canopy (e.g. its density) and the parameters of the mixing layer.

In order to understand if the closure adopted for the $Re = O(1)$ case in (2.24) makes sense we have used the experimental data of Ghisalberti & Nepf (2004) where a fully developed turbulent flow of water over a submerged layer of vertical rigid fibres is studied. The setting of the problem is sketched in figure 19; the porosity ϑ in the experiments ranges from 0.96 to 0.99 and ε is approximately 0.2 (defined as the ratio between the diameter of the fibres and the height of the water column). The measurements of the mean velocity inside the canopy and the driving term are available so that the permeability $\mathscr{K}_{11}$ can be estimated *a posteriori* using Darcy's law which, in this case, can be written in dimensional variables as

$$\langle u_1^{(0)} \rangle = \mathscr{K}_{11} \frac{g \sin \alpha}{\nu}, \qquad (5.1)$$

where $\nu = 0.94 \times 10^{-6}$ m^2 s^{-1} is deduced using Re_{ml} in table 1 of Ghisalberti & Nepf (2004) and α is the slope of the inclined system. The use of (5.1) in the lower zone
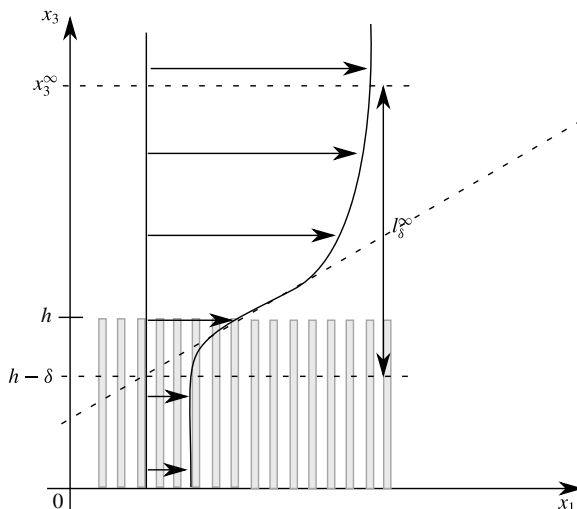
FIGURE 19. Setting of the experiments of Ghisalberti & Nepf (2004). Water flows over a layer of rigid cylindrical fibres. The whole system is slightly inclined at an angle α so that the fluid motion is driven by gravity.

of the canopy, termed 'wake zone', is justified on physical grounds since, as noted by Ghisalberti & Nepf (2009), such a region is 'governed by a simple balance of drag and hydraulic gradient, much like classical porous medium flow'.

Figures 20 and 21 display results for the microscopic permeability field K_{11} within the elementary volume, and the averaged values $\mathscr{K}_{11}$ for variable pore velocity. The grey band represents the range of permeability $\mathscr{K}_{11}$ computed using the homogenized model (2.24) for the corresponding porosities of each experiment. The experimental values are in reasonably good agreement with the homogenized values; discrepancies are of the same order as those shown in figure 6 and table 1.

We now consider the problem from a macroscopic point of view. Observing the sketch of the velocity profile in figure 19 it seems reasonable to impose continuity of the streamwise velocity at a distance δ (the penetration depth) below the top of the canopy. This is the fictitious interface and (5.1) is thus applicable for $x_3 \in [0, h - \delta]$. Since we are dealing with a fully developed turbulent flow, in the region above the fictitious interface ($x_3 \in [h - \delta, x_3^\infty]$), after using the Reynolds decomposition for the velocity (i.e. $u_i = U_i + u_i'$) plus temporal averaging ($\bar{\cdot}$), the streamwise momentum equation reads:

$$\frac{\partial \overline{u_1' u_3'}}{\partial x_3} = g \sin \alpha. \tag{5.2}$$

Thus, the turbulent stress balances the hydraulic gradient in the upper zone (termed the 'exchange zone'), whereas the viscous term can be neglected. Assuming a constant mixing length model, such as that proposed by Ghisalberti & Nepf (2004), the Reynolds stress can be written as

$$-\overline{u_1' u_3'} = \left(c l_\delta^\infty \frac{\partial U_1}{\partial x_3} \right)^2, \tag{5.3}$$
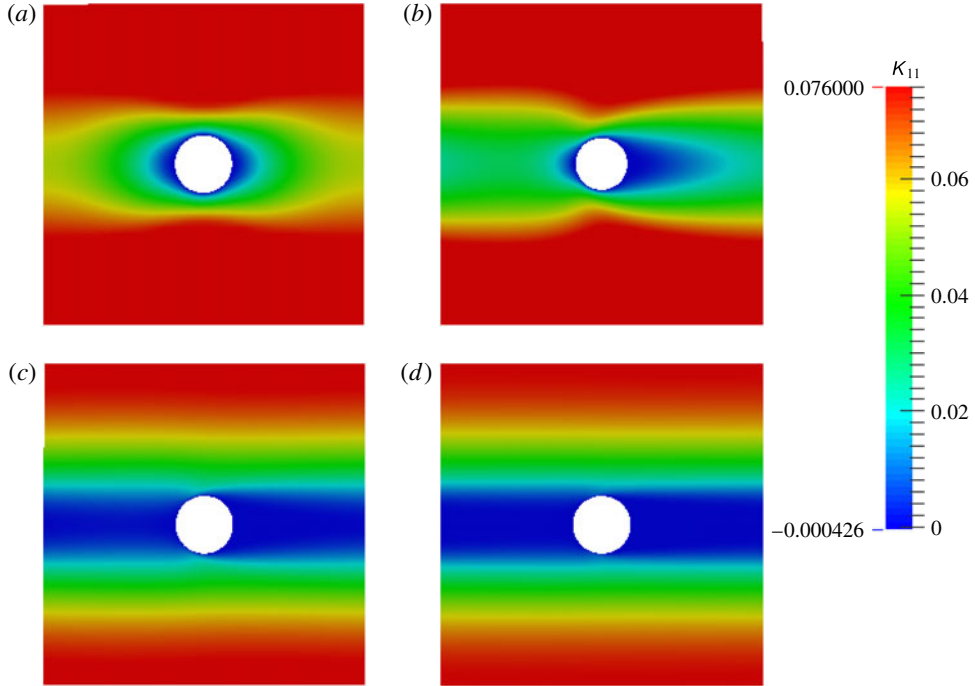
FIGURE 20. (Colour online) Horizontal component of the permeability K_{11} within a unit cell, for varying $\vartheta Re_p = 0, 50, 500, 1500$. Increasing Re_p, the value of K_{11} is reduced and the distribution initially loses symmetry with respect to the vertical mid-plane through the cylinder, to eventually regain it because of periodicity for ϑRe_p above 500. Here $\vartheta = 0.975$.

where l_δ^∞ is shown in figure 19, c is a constant and their product is a 'mixing length'. Substituting (5.3) into (5.2) and solving for the mean flow it is found:

$$U_1(x_3) = U_1(h - \delta) + \frac{2}{3} \frac{\sqrt{g \sin \alpha}}{c l_\delta^\infty} [(x_3^\infty - h + \delta)^{3/2} - (x_3^\infty - x_3)^{3/2}]. \qquad (5.4)$$

The condition at the fictitious interface yields $U_1(h - \delta) = \langle u_i^{(0)} \rangle (h - \delta) = \mathscr{K}_{11}(g \sin \alpha / \nu)$. As we can observe from figure 22 the proposed solution fits the experiments with the unique value of $c = 0.086$. Summing up, we can make the following two points:

(i) The values of the permeability deduced from the experiments slightly overestimate those evaluated via homogenization theory (cf. figure 21), and this is possibly due to the fact that in the experiments by Ghisalberti & Nepf (2004) the parameter ϵ is approximately 0.2, a value which is not much smaller than one.

(ii) The agreement between the experimental and theoretical velocity profiles in figure 22 confirms that the interface condition A of Le Bars & Worster (2006) is suitable in this turbulent case. Moreover, for the four experiments analysed, the order of magnitude of δ estimated from (3.3) matches that used here. However, if c in (3.3) were a simple constant, considering the trend of $\mathscr{K}_{11}$ in figure 21, δ would decrease for increasing values of Re_p, contrary to observations (cf. the inset
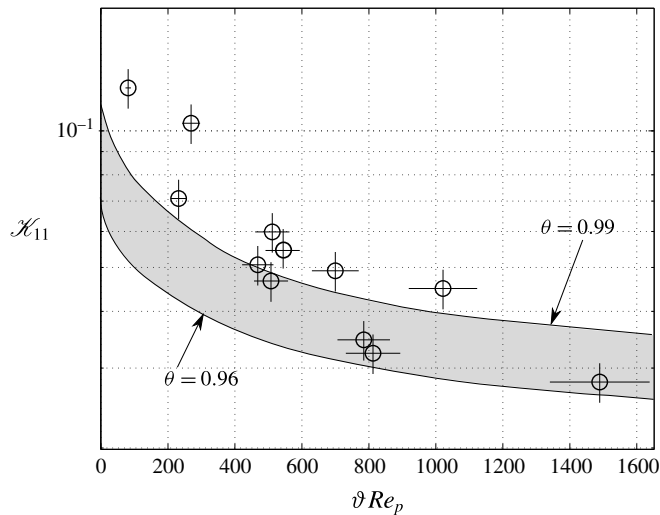
FIGURE 21. Horizontal component of the permeability $\mathcal{K}_{11}$ versus ϑRe_p of (2.24) from the measurements by Ghisalberti & Nepf (2004). Since the permeability is deduced from experimental data, the vertical and horizontal bars represent the uncertainty of the measurements which is approximately 10 % for each value. The grey band represents the range of permeabilities calculated by the homogenized model for finite Reynolds numbers for $0.96 \leqslant \vartheta \leqslant 0.99$.

in figure 22). Thus, the 'constant' c in (3.3) should be rendered an increasing function of Re_p for δ to increase monotonically with the increase of the pore velocity (at each given value of θ).

6. Conclusions

A homogenization approach has been used to study the flow over and through a orthotropic porous medium. The work is developed essentially from two points of view: the microscopic and the macroscopic ones. The microscopic equations provide a characterization of the particular geometry of the porous medium, resulting in an estimate for the components of the permeability tensor; only two diagonal components of this second-order tensor are present in the particular medium considered since the terms relative to the plane normal to the fibres' axes are equal. This result can be easily confirmed analytically (Milton 2004). Since we are interested in the macroscopic field, the permeability tensor is averaged over the elementary cell and the values $\mathcal{K}_{11}$ and $\mathcal{K}_{33}$ are compared with values from the literature, obtaining good agreement. A new correlation for the (scalar) permeability $\mathcal{K}$ of an isotropic medium is also provided as a function of the porosity ϑ of the medium, correcting the classical relation by Kozeny–Carman.

In the presence of inertia within the porous region, an approach to estimate the permeability is proposed, based on the Oseen linearization of the equations in the unit cell, plus an iterative approach which alternates between the microscopic and the macroscopic regions. With this technique, the apparent permeability from the theory approaches the values found in experiments and DNS, with the correct trend as a function of the pore Reynolds number. The theoretical values do not precisely
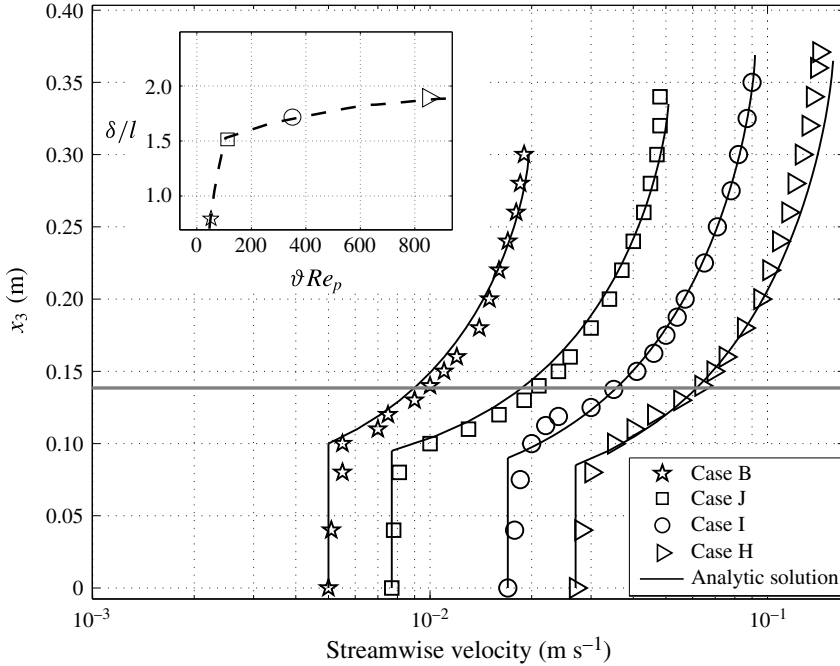
FIGURE 22. Analytical velocity profiles, in dimensional variables, against experimental results by Ghisalberti & Nepf (2004, 2006, 2009) for turbulent flow over a layer of rigid fibres. The symbols represent the velocity measurements (with uncertainty of 5 %) for cases B, H, I and J of table 1 of Ghisalberti & Nepf (2004). The analytical solution, (5.4), is represented by the solid lines. Two horizontal grey lines, which appear overlapped in the scale of the figure, represent the physical interface h (in dimensional terms $h = 0.139$ m for case B and $h = 0.138$ m for the other cases). In the inset the values of δ, which define the fictitious interface at $x_3 = h - \delta$, are shown for the corresponding cases. The dashed line is drawn to guide the eye. In the four experiments we have used the following values for l_δ^∞: ☆: 0.202 m □: 0.245 m ○: 0.279 m ▷: 0.286 m. Furthermore, the microscale l (used to normalize δ in the inset) is equal to 5.06 cm in experiment B (with $\vartheta = 0.99$) and 2.83 cm in the other cases (for which $\vartheta = 0.96$).

match those available from experiments or DNS because the fibres considered here are neither sufficiently slender nor packed densely enough for the first-order equations of the multiple scale approximation to be fully adequate. To improve this, one could possibly push the multiple scale theory up to higher order.

The coupling of the flow problem within the porous medium with that in a pure fluid region neighbouring it is particularly important and different interface conditions have been evaluated. All of them contain some degree of arbitrariness and parameters which must be tuned. The main conclusion here is that Darcy's law provides a good approximation of the velocity inside the porous medium, also when inertia in the flow within the P-region is non-negligible. The interface condition of Le Bars & Worster (2006), which is an extension of the one by Beavers & Joseph (1967), is found to be the most suitable, both in the case of laminar and turbulent flow. The penetration depth δ which needs to be imposed satisfies the order estimate of Le Bars & Worster (2006), for fixed pore Reynolds number. When ϑRe_p increases also δ increases, and this should be accounted for when selecting δ in the model.

Conversely, the use of Brinkman's correction to Darcy's law should be avoided when the porosity is not large since, on the one hand, the value of the effective viscosity μ_e is uncertain and, on the other, results with this model appear to systematically overestimate the velocity near the interface between the fluid and the porous domain.

Finally, also a condition which employs permeability components which vary as the interface is approached do not appear adequate. The distance over which the permeability approaches the infinite value of the pure fluid region has been estimated to be of order ϵ on the basis of DNS, and depends mildly on Reynolds number, for the range considered which spans three orders of magnitude. The use of permeability components which change smoothly (even according to DNS results) is, however, not sufficient in a coupled NSE–Darcy system to represent inertial effects within a small porous layer adjacent to the pure fluid region, and this suggests the inclusion of a Forchheimer term in a thin-layer interface model (Firdaouss *et al.* 1997).

Future work will focus on the flow of fluid over and through a bundle of flexible fibres.

Acknowledgements

REFERENCES

ANGOT, P., BRUNEAU, C. H. & FABRIE, P. 1999 A penalization method to take into account obstacles in incompressible viscous flows. *Numer. Math.* **81** (4), 497–520.

AURIAULT, J. L. 2009 On the domain of validity of Brinkman's equation. *Trans. Porous Med.* **79** (2), 215–223.

BATTIATO, I. 2012 Self-similarity in coupled Brinkman/Navier–Stokes flows. *J. Fluid Mech.* **699**, 94–114.

BEAVERS, G. S. & JOSEPH, D. D. 1967 Boundary conditions at a naturally permeable wall. *J. Fluid Mech.* **30** (1), 197–207.

BREUGEM, W. P. & BOERSMA, B. J. 2005 Direct numerical simulations of turbulent flow over a permeable wall using a direct and a continuum approach. *Phys. Fluids* **17**, 025103.

BREUGEM, W. P., BOERSMA, B. J. & UITTENBOGAARD, R. E. 2004 Direct numerical simulations of plane channel flow over a 3D cartesian grid of cubes. *Appl. Porous Media (ICAPM 2004)* 27–35.

BRINKMAN, H. C. 1949 A calculation of the viscous force exerted by a flowing fluid on a dense swarm of particles. *Appl. Sci. Res.* **1** (1), 27–34.

BRUNEAU, C. H. & MORTAZAVI, I. 2008 Numerical modelling and passive flow control using porous media. *Comput. Fluids* **37** (5), 488–498.

CARMAN, P. C. 1939 Permeability of saturated sands, soils and clays. *J. Agric. Sci.* **29** (2), 262–273.

CARRARO, T., GOLL, C., MARCINIAK-CZOCHRA, A. & MIKELIĆ, A. 2013 Pressure jump interface law for the Stokes–Darcy coupling: confirmation by direct numerical simulations. flows. *J. Fluid Mech.* **732**, 510–536.

CARRARO, T., GOLL, C., MARCINIAK-CZOCHRA, A. & MIKELIĆ, A. 2015 Effective interface conditions for the forced infiltration of a viscous fluid into a porous medium using homogenization. *Comput. Meth. Appl. Mech. Engng* **292**, 195–220.

CHANDESRIS, M. & JAMET, D. 2008 Jump conditions and surface-excess quantities at a fluid/porous interface: a multi-scale approach. *Trans. Porous Med.* **78**, 419–438.

CIMOLIN, F. & DISCACCIATI, M. 2013 Navier–Stokes/Forchheimer models for filtration through porous media. *Appl. Numer. Maths* **72**, 205–224.

DARCY, H. 1856 *Les Fontaines Publiques de la Ville de Dijon*. Victor Dalmont.

DAVIT, Y., QUINTARD, M., BELL, C. G., BYRNE, H. M., CHAPMAN, L. A. C., KIMPTON, L. S., LANG, G. E., OLIVER, J. M., PEARSON, N. C., WATERS, S. L. *et al.* 2013 Homogenization via formal multiscale asymptotics and volume averaging: How do the two techniques compare? *Adv. Water Resour.* **62**, 178–206.

EDWARDS, D. A., SHAPIRO, M., BAR-YOSEPH, P. & SHAPIRA, M. 1990 The influence of Reynolds number upon the apparent permeability of spatially periodic arrays of cylinders. *Phys. Fluids* **2** (1), 45–55.

ENE, H. I. & SÁNCHEZ-PALENCIA, E. 1975 Equations et phénomènes de surface pour l' écoulement dans un modèle de milieu poreux. *J. Méc.* **14**, 73–108.

FINNIGAN, J. J. 2000 Turbulence in plant canopies. *Annu. Rev. Fluid Mech.* **32**, 519–571.

FIRDAOUSS, M., GUERMOND, J. & LE QUÉRÉ, P. 1997 Nonlinear correction to Darcy's law at low Reynolds numbers. *J. Fluid Mech.* **343**, 331–350.

GHISALBERTI, M. & NEPF, H. M. 2004 The limited growth of vegetated shear layers. *Water Resour. Res.* **40** (7), 1–12.

GHISALBERTI, M. & NEPF, H. M. 2006 The structure of the shear layer over rigid and flexible canopies. *Environ. Fluid Mech.* **6** (3), 277–301.

GHISALBERTI, M. & NEPF, H. M. 2009 Shallow flows over a permeable medium: the hydrodynamics of submerged aquatic canopies. *Trans. Porous Med.* **78** (2), 309–326.

GIVLER, R. C. & ALTOBELLI, S. A. 1994 A determination of the effective viscosity for the Brinkman–Forchheimer flow model. *J. Fluid Mech.* **258**, 355–370.

GRAY, W. G. 1975 A derivation of the equations for multi-phase transport. *Chem. Engng Sci.* **30** (2), 229–233.

GUSTAFSSON, J. & PROTAS, B. 2013 On Oseen flows for large Reynolds numbers. *Theor. Comput. Fluid Dyn.* **27** (5), 665–680.

HILL, A. A. & STRAUGHAN, B. 2008 Poiseuille flow in a fluid overlying a porous medium. *J. Fluid Mech.* **603**, 137–149.

JACKSON, G. W. & JAMES, D. F. 1986 The permeability of fibrous porous media. *Can. J. Chem. Engng* **64** (3), 364–374.

JÄGER, W. & MIKELIĆ, A. 1996 On the boundary conditions at the contact interface between a porous medium and a free fluid. *Annali Scuola Normale Superiore di Pisa, Classe di Scienze-Serie IV*, vol. 23, pp. 403–465.

JÄGER, W. & MIKELIĆ, A. 2000 On the interface boundary condition of Beavers, Joseph, and Saffman. *SIAM J. Appl. Maths* **60** (4), 1111–1127.

JAMES, D. F. & DAVIS, A. M. J. 2001 Flow at the interface of a model fibrous porous medium. *J. Fluid Mech.* **426**, 47–72.

JAMET, D. & CHANDESRIS, M. 2009 On the intrinsic nature of jump coefficients at the interface between a porous medium and a free fluid region. *Intl J. Heat Mass Transfer* **52**, 289–300.

KAVIANY, M. 1995 *Principles of Heat Transfer in Porous Media*. Springer.

KUTTANIKKAD, S. P. 2009 Pore-scale direct numerical simulation of flow and transport in porous media. PhD thesis, Ruprecht-Karls-Universität Ruprecht-Karls-Universität, Heidelberg, Germany.

LE BARS, M. & WORSTER, M. 2006 Interfacial conditions between a pure fluid and a porous medium: implications for binary alloy solidification. *J. Fluid Mech.* **550** (1), 149–173.

MARCINIAK-CZOCHRA, A. & MIKELIĆ, A. 2012 Effective pressure interface law for transport phenomena between an unconfined fluid and a porous medium using homogenization. *Multiscale Model. Simul.* **10** (2), 285–305.

MATSUMURA, Y. & JACKSON, T. L. 2014 Numerical simulation of fluid flow through random packs of cylinders using immersed boundary method. *Phys. Fluids* **26** (4), 043602.

MEI, C. C. & AURIAULT, J. L. 1991 The effect of weak inertia on flow through a porous medium. *J. Fluid Mech.* **222**, 647–663.

MEI, C. C. & VERNESCU, B. 2010 *Homogenization Methods for Multiscale Mechanics*. World Scientific.

MILTON, G. W. 2004 *The Theory of Composites*. Cambridge University Press.

MITYUSHEV, V. & ADLER, P. M. 2002*a* Longitudinal permeability of spatially periodic rectangular arrays of circular cylinders I: a single cylinder in the unit cell. *Z. Angew. Math. Phys.* **82** (5), 335–346.

MITYUSHEV, V. & ADLER, P. M. 2002*b* Longitudinal permeability of spatially periodic rectangular arrays of circular cylinders II: an arbitrary distribution of cylinders inside the unit cell. *Z. Angew. Math. Phys.* **53** (3), 486–514.

NEPF, H. M. 2012 Flow and transport in regions with aquatic vegetation. *Annu. Rev. Fluid Mech.* **44**, 123–142.

OCHOA-TAPIA, J. A. & WHITAKER, S. 1995 Momentum transfer at the boundary between a porous medium and a homogeneous fluid. I: theoretical development. *Intl J. Heat Mass Transfer* **38** (14), 2635–2646.

PEROT, J. B. 1993 An analysis of the fractional step method. *J. Comput. Phys.* **108**, 51–58.

QUARTERONI, A. & VALLI, A. 1999 *Domain Decomposition Methods for Partial Differential Equations*. Oxford University Press.

QUINTARD, M. & WHITAKER, S. 1994 Transport in ordered and disordered porous media II: generalized volume averaging. *Trans. Porous Med.* **14** (2), 179–206.

RAUPACH, M. R., FINNIGAN, J. J. & BRUNET, Y. 1996 Coherent eddies and turbulence in vegetation canopies: the mixing-layer analogy. *Boundary-Layer Meteorol.* **78**, 351–382.

SADIQ, T. A. K., ADVANI, S. G. & PARNAS, R. S. 1995 Experimental investigation of transverse flow through aligned cylinders. *Intl J. Multiphase Flow* **21** (5), 755–774.

SAFFMAN, P. G. 1971 Boundary condition at the surface of a porous medium. *Stud. Appl. Maths* **50** (2), 93–101.

SAHRAOUI, M. & KAVIANY, M. 1992 Slip and no–slip velocity boundary conditions at interface of porous, plain media. *Intl J. Heat Mass Transfer* **35** (4), 927–943.

SANGANI, A. S. & YAO, C. 1988 Transport processes in random arrays of cylinders. II: viscous flow. *Phys. Fluids* **31** (9), 2435–2444.

SKARTSIS, L. & KARDOS, J. L. 1990 The Newtonian permeability and consolidation of oriented carbon fiber beds. In *Proceedings of the American Society for Composites. Fifth Technical Conference: Composite Materials in Transition. East Lansing, MI*, pp. 548–556.

SKJETNE, E. & AURIAULT, J. L. 1999 New insights on steady, non-linear flow in porous media. *Eur. J. Mech.* (B/*Fluids*) **18** (1), 131–145.

TAMAYOL, A. & BAHRAMI, M. 2009 Analytical determination of viscous permeability of fibrous porous media. *Intl J. Heat Mass Transfer* **52** (9), 2407–2414.

VAN DER WESTHUIZEN, J. & DU PLESSIS, J. P. 1996 An attempt to quantify fibre bed permeability utilizing the phase average Navier–Stokes equation. *Composites* A **27** (4), 263–269.

WHITAKER, S. 1986 Flow in porous media I: a theoretical derivation of Darcy's law. *Trans. Porous Med.* **1** (1), 3–25.

WHITAKER, S. 1996 The Forchheimer equation: a theoretical development. *Trans. Porous Med.* **25** (1), 27–61.

WHITAKER, S. 1998 *The Method of Volume Averaging*. Jacob Bear, Technion – Israel Institute of Technology.

YAZDCHI, K., SRIVASTAVA, S. & LUDING, S. 2011 Microstructural effects on the permeability of periodic fibrous porous media. *Intl J. Multiphase Flow* **37** (8), 956–966.

ZAMPOGNA, G. A. 2016 Homogenized-based modeling of flows over and through poroelastic media, PhD thesis, University of Genova, Italy.

ZICK, A. A. & HOMSY, G. M. 1982 Stokes flow through periodic arrays of spheres. *J. Fluid Mech.* **115**, 13–26.